Direct Numerical Simulation of Hypersonic Flow over a Blunt Cone with Axisymmetric Isolated Roughness

Christopher Haley* and Xiaolin Zhong†
University of California, Los Angeles, CA 90095, USA

The ability of a finite roughness element to suppress the hypersonic second-mode instability on a cone is explored. A new code for simulating discrete roughness using a body-fitted grid over an analytic shape is developed. Linear stability analysis is performed on the Mach 8 meanflow of a 7° half-angle straight cone. The resulting N-factor analysis determines the second-mode frequency of 240 kHz to most likely to lead to turbulent transition. A phase velocity plot of the hypersonic modes is obtained and the resulting synchronization location of s=0.2436 meters is determined. This led to the design and placement of a roughness element that will effectively suppress the targeted disturbance frequency. An unsteady simulation with a blowing-suction actuator, upstream of the roughness element, introduces a pulse with a nominal frequency content up to 1 MHz. FFT's of the pulse's history for a roughness case and a no-roughness case are computed and compared. Frequencies 218 kHz and higher are suppressed while lower frequencies are amplified, effectively showing that the roughness element is able to suppress the target disturbance frequency.

I. Introduction

Understanding high speed laminar-turbulent boundary-layer transition is a long standing goal of hypersonic research. Considerable progress has been made in the past decades by parsing out the problem into areas of receptivity, linear growth, and nonlinear breakdown. But complete knowledge of the underlying mechanisms remain elusive.[1] Meanwhile, the undesired consequences of boundary-layer transition such as increased drag and surface heating on hypersonic vehicles remain. Surface heating is especially problematic for the development of such vehicles, and advocates for a means to predict and ultimately control the onset of boundary-layer transition. Computational and experimental research into using 2-D finite roughness strips to delay the onset of transition has shown considerable promise.[2–4] To further this research, this paper presents a newly developed direct numerical simulation (DNS) code to explore the effect surface roughness on the transition process on a hypersonic cone. Additionally, a simulation of an axisymmetric isolated roughness strip and its effect on laminar-turbulent transition is explored.

Ongoing research has identified several factors that affect the transition process, this includes, among others, receptivity of freestream disturbances, nose bluntness, surface temperature, and isolated and distributed roughness. Of particular interest is the effect isolated roughness has on transition. Surface roughness is typically classified in terms of its height with respect to the boundary layer. Heights that expedite natural transition or cause its immediate onset are often termed 'critical' or 'effective' respectively. However there are unique instances where a height counterintuitively delays transition. A growing body of computational evidence by Fong and Zhong[2,3] is fast proving the existence of this sub-critical phenomenon. The most compelling of which is a collaborative effort with Dr. Steven Schneider at Purdue[4] in which a transition-delaying roughness experiment is designed according to the passive laminar control method patented by Zhong and Fong.[5]

Prior to these recent investigations by Fong, there have been reports of experiments encountering the transition-delaying effect. The first was in 1959 by James who noted that for a given Mach number, an optimum value of roughness height was found which gave a maximum laminar run.[6] In 1964, Holloway and

*Graduate Research Assistant, Mechanical and Aerospace Engineering Department, clhaley@g.ucla.edu.
†Professor, Mechanical and Aerospace Engineering Department, AIAA associate fellow

Sterrett found in Mach 4.0 and 6.0, that under certain circumstances roughness with a height less than the boundary layer thickness can delay transition.[7] More recently, Fujii found experimentally that 2-D wavy wall roughness can delay transition.[8] Also in 2014, Chynoweth et. al. looked at 3-D isolated roughness in which at a certain heights were found to interact with the second mode without tripping the boundary layer.[9]

The simulation utilized in this paper is based on a collaborative DNS/experimental study with Dr. Katya Casper at Sandia National Laboratories (SNL). The computational work was carried out to design a transition delaying arrangement of roughness elements to be validated experimentally. The experiment consists of a Mach 8 straight blunt cone with axisymmetric roughness elements arranged in a streamwise pattern, similar to the computational/experimental collaboration previously done with Dr. Schneider's Lab.[4] The computational work in this previous collaboration, however, used observations of second-mode suppression taken from a flat plate simulation and, in conjunction with a cone meanflow simulation, extended the flat plate observations to a compression cone boundary-layer in order to design the transition delaying arrangement. No simulation of a roughness element on a cone was actually undertaken. With the development of the code detailed in this paper, the meanflow and unsteady simulations of a finite roughness element on a straight blunt cone can now be computed completely.

Regarding the collaboration with Dr. Casper, the simulation detailed in this paper was computed using the code. In order to design the transition-delay roughness element, the computational work had to identify the second-mode frequency most likely to lead to transition and the synchronization location (the location where the phase velocity of mode F and mode S are equal) of said frequency. From this information a roughness element is designed and placed on the cone. An unsteady simulation of the roughness on the cone is computed. FFT analysis of the unsteady pressure perturbations determines which frequencies are being suppressed by the roughness element. Currently, only a single axisymmetric roughness strip is considered in this simulation.

II. Governing Equation and Computational Methodology

The DNS code utilized in this paper is a 5^{th}-order code that uses shock-fitting to accurately compute the location of the bow shock on a straight blunt cone geometry. This base geometry and high-order shock-fitting approach has been validated extensively for accuracy.[10] The roughness element is implemented by taking an analytical shape, in this case the difference of two hyperbolic tangents and mapping it to the surface geometry. In order for the mapping to work the function of the analytical shape must go to zero beyond the initial shape. By this approach, a global 5^{th}-order accuracy for the entire problem is maintained, making it suitable for unsteady simulations.

A. Governing Equations

The DNS code solves the conservation-law form of the three-dimensional Navier-Stokes equations in Cartesian coordinates. Written in vector form, the governing equations are

$$\frac{\partial U}{\partial t} + \frac{\partial F_j}{\partial x_j} + \frac{\partial F_{v,j}}{\partial x_j} = 0 \tag{1}$$

in which U is the state vector of conserved quantities, and F_j and $F_{v,j}$ are the inviscid flux and viscous flux in the j^{th} spatial direction respectively,

$$U = \{\rho,\ \rho u_1,\ \rho u_2,\ \rho u_3,\ e\}^T \tag{2}$$

$$F_j = \{\rho u_j,\ \rho u_1 u_j + p\delta_{1j},\ \rho u_2 u_j + p\delta_{2j},\ \rho u_3 u_j + p\delta_{3j},\ (e+p)u_j\}^T \tag{3}$$

$$F_{v,j} = \{0,\ \tau_{1j},\ \tau_{2j},\ \tau_{3j},\ \tau_{jk}u_k - q_j\}^T \tag{4}$$

The internal energy, e, shear stress, τ_{ij}, and heat flux, q_j, are given as follows,

$$e = \rho\left(c_v T + \frac{u_k u_k}{2}\right) \tag{5}$$

$$\tau_{ij} = \mu\left(\frac{\partial u_i}{\partial x_j} + \frac{\partial u_j}{\partial x_i}\right) + \delta_{ij}\lambda\frac{\partial u_k}{\partial x_k} \tag{6}$$

$$q_j = -\kappa \frac{\partial T}{\partial x_j} \tag{7}$$

For the simulation under consideration, the properties of nitrogen gas are used. This is consistent with the facilities at SNL and the experimental conditions this simulation is patterned after. Thus, a calorically perfect gas is assumed to close Eq. (1),

$$p = \rho R T \tag{8}$$

A specific gas constant of $R = 296.8 J/kgK$ for nitrogen gas is used. And the specific heats c_p and c_v are held constant with a given specific heats ratio of $\gamma = 1.4$. Moreover, the viscosity coefficient, μ, is calculated by Sutherland's law in the form:

$$\mu = \mu_r \left(\frac{T}{T_o}\right)^{3/2} \frac{T_o + T_s}{T + T_s} \tag{9}$$

where $\mu_r = 1.7894 \times 10^{-5}$ N·s/m^2, $T_o = 288.0$ K, and $T_s = 110.33$ K. Lastly, λ is taken as $-2/3\mu$ and the thermal conductivity, κ, is computed from the constant Prandtl number,

$$\kappa = \frac{c_p \mu}{Pr} \tag{10}$$

Fong and Zhong,[2] Huang and Zhong,[11] and Lei and Zhong[12] have used the same formulation or similar formulations for simulating perfect gas hypersonic flow.

B. Shock-fitting Method

A shock-fitting method is used to obtain a defined shock location. The shock-fitting method treats the shock as the upper boundary of the physical domain by computing the location of the bow shock produced by the blunt cone. Hence, the physical domain of the simulation is defined by the bow shock from above and the cone surface below. Eq. (1) is solved in a computational domain with body fitted curvilinear coordinates (ξ, η, ζ, τ), where ξ is in the direction of the cone surface, η is normal to the cone surface, ζ is in the azimuthal direction, and τ is time. Treating the shock as a domain boundary, the transient shock movement is solved as an ODE alongside the governing equation. Thus, in the computational domain surfaces of constant η are unsteady due to shock movement, while surfaces of constant ξ and ζ are fixed. Therefore, the transformation relations between the physical domain and computational domain are

$$\begin{cases} \xi = \xi(x,y,z) \\ \eta = \eta(x,y,z,t) \\ \zeta = \zeta(x,y,z) \\ \tau = t \end{cases} \Leftrightarrow \begin{cases} x = x(\xi,\eta,\zeta,\tau) \\ y = y(\xi,\eta,\zeta,\tau) \\ z = z(\xi,\eta,\zeta,\tau) \\ t = \tau \end{cases} \tag{11}$$

Details of transforming Eq. (1) into the computational domain can be found in Zhong, 1998.[10]

As mentioned above, the shock-fitting method treats the bow shock as a computational boundary at

$$\eta(x,y,z,t) = \eta_{max} = constant. \tag{12}$$

Accordingly, functions for the shock position and velocity must be obtained of the form $H(\xi,\zeta,\tau)$ and $H_\tau(\xi,\zeta,\tau)$ and solved as independent flow variables alongside the governing equations. Stated simply, this can be done by taking the Rankine-Hugoniot relations, which provide the flow variable boundary conditions behind the shock, as a function of U_∞ and the velocity of the shock front v_n. The shock front velocity is determined by a characteristic compatibility equation at the grid point immediately behind the shock. A complete derivation of H and H_τ can also be found in Zhong, 1998.[10]

Lastly, an explicit 5^{th} order finite-difference method is used to discretize the transformed governing equations, H, and H_τ in the ξ and ζ-directions. A spectral scheme is used for derivatives in the η-direction for axisymmetric cases and finite-difference is used in non-axisymmetric cases. Meanflow simulations are advanced using Euler's method (RK-1) for speed of computation.

C. Discrete Body-fitted Roughness

The discrete surface roughness elements in this paper is implemented by mapping the function of an analytical shape to the cones frustum. Choosing the shape of said function allows for a degree of creativity, but the function must be compatible with the grid transformation, Eq. (11). The use of grid metrics requires that the shape have a continuous derivative throughout the domain. As a consequence sharp edged geometries such as diamonds or squares are not possible. Such geometries can be implemented using a finite volume or immersed interface method approach but at the cost of losing high-order accuracy around the roughness element. By limiting the geometry to analytical shapes, the high-order accuracy of our solution is maintained. In this paper, the roughness shape is defined as the difference of two hyperbolic tangents,

$$y'(x', z') = \frac{1}{2}h\left\{\tanh\left[q\left(x' + \frac{w}{2}\right)\right] - \tanh\left[q\left(x' - \frac{w}{2}\right)\right]\right\} \tag{13}$$

where x', y', and z' are Cartesian coordinates prior to being mapped to the cone surface. The parameters h and w control the height and width of the roughness and q is a free parameter that controls the edge steepness.

Equation (13) is mapped to the cones frustum using the following rotation and translation equations,

$$\begin{aligned} x &= cos(\theta_{\frac{1}{2}})x' - sin(\theta_{\frac{1}{2}})y' + x_c \\ y &= [sin(\theta_{\frac{1}{2}})x' + cos(\theta_{\frac{1}{2}})y' + y_c]cos(\theta) \\ z &= [sin(\theta_{\frac{1}{2}})x' + cos(\theta_{\frac{1}{2}})y' + y_c]sin(\theta) \end{aligned} \tag{14}$$

in which x, y, and z are the Cartesian coordinates in the physical domain, $\theta_{\frac{1}{2}}$ is the cone half-angle, θ is the angle in the azimuthal direction about the cone, and x_c and y_c is the surface location of the roughness center at $\theta = 0$.

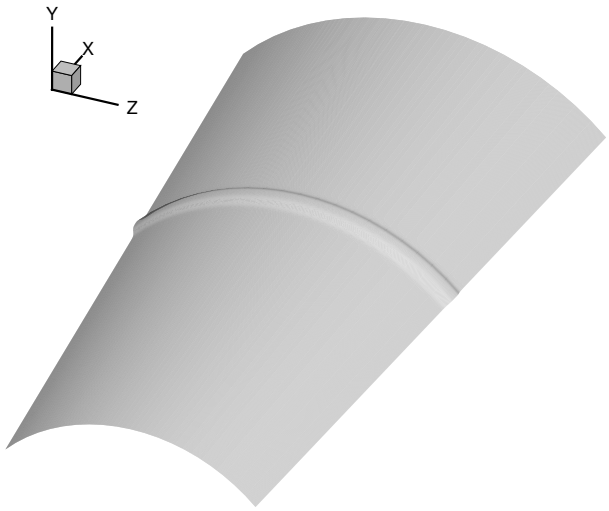

Figure 1: Roughness shape generated by Eq. (13) for $q = 1500$ after being mapped to a cone surface.

Figure 1 plots Eq. (13) as it would appear on a cone frustum. The figure shows that applying Eq. (14) produces a circumferential roughness. This surface geometry is similar to that used in the Purdue experiment.[4] Investigations of the roughness effect, thus far, have only investigated the importance of an elements overall height and width with little attention paid to the physical geometry (e.g. elliptical strips vs. square strips). Experiments and simulations with comparable results but different shapes suggests the physical geometry has little bearing on the suppression effect when compared to overall height.[3,4]

D. Direct Numerical Simulation of Disturbances

To simulate unsteady disturbances, a blowing-suction actuator is use to introduce a pulse into a resolved meanflow with surface roughness. The actuator extends circumferentially around the cone and is placed

upstream of the roughness element. The pulse has a Gaussian shape in time and is sinusoidal in space. The sinusoid shape avoids introducing additional mass into the mean flow. The frequency spectrum of the pulse is chosen to be broad enough as to include the most unstable mode frequencies for the given flow conditions. Downstream of the roughness, the frequencies are examined for roughness induced amplification or suppression. This technique of using a Gaussian pulse to examine mode amplification/suppression was previously implemented by Fong et al.[13]

Equation (15) below is the function used to generate the unsteady pulse,

$$v_p(x,t) = 10^{-3}U_\infty exp\left(\frac{-(t-\mu)^2}{2\sigma^2}\right) sin\left(2\pi\frac{x-x_s}{l}\right) \tag{15}$$

for $x_s < x < x_s + l$ and $t > 0$. In which μ is the mean, σ is the standard deviation, x_s is the starting location for the actuator, and l is the length of the actuator. The peak amplitude of the pulse is scaled as $10^{-3}U_\infty$. The mean of the pulse is defined in terms of velocity 'tolerance', v_{tol}, which is the initial pulse velocity at t=0. Naturally, v_{tol} is very small, preferably close to zero, however not too small that an appreciable amount of computational time passes before the pulse is fully developed. The equation for μ is given as,

$$\mu = \sqrt{-2\sigma^2 ln\left(\frac{v_{tol}}{10^{-3}U_\infty}\right)}. \tag{16}$$

By defining μ in this way, μ can be fixed with a reasonable v_{tol} regardless of the simulation conditions. Thus, by design, the only remaining free parameter in Eq. (15) is σ which permits direct control over the frequency content of the pulse. Hence, when designing the pulse for a particular case, only the standard deviation needs to be modified. The pulse parameters used in this paper are given in Table 1, moreover the time history of Eq. (15) and its corresponding FFT are given in Fig. 2.

Table 1: Pulse parameters

Parameter	Value	Unit
$10^{-3}U_\infty$	1.0931	m/s
v_{tol}	10^{-10}	m/s
σ	0.3	μs
μ	2.0398	μs
x_s	0.1976	m
l	1.9703	mm

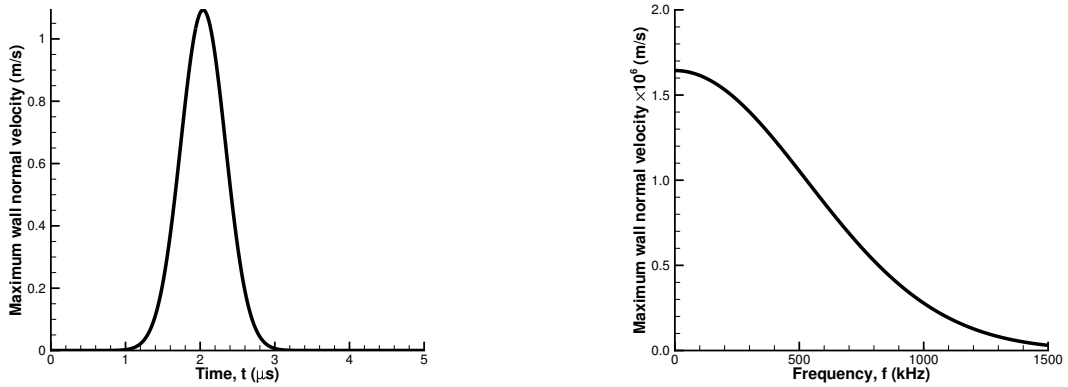

(a) (b)

Figure 2: (a) Time history of the maximum wall normal velocity. (b) FFT of maximum wall normal velocity in (a).

E. Simulation Approach

The process for DNS of surface roughness in unsteady flow starts with computing the converged meanflow of the smooth surface case. A roughness element is then added to the converged smooth meanflow and the meanflow for this case is computed. In order to guide the design of the roughness element, a stability analysis of the smooth meanflow is performed using linear stability theory (LST).[14] With both converged meanflows in hand, the blowing-suction actuator is added and the unsteady simulation is computed. FFT is performed on the unsteady results and the cases are compared.

III. Freestream and Simulation Conditions

As previously mentioned, the simulation is based on a straight blunt cone geometry at zero angle-of-attack. The cone has a 7° half-angle and a nose radius of 0.5 mm with a total length of 0.534 m measured from the blunt nose tip. The simulation is axisymmetric. The freestream conditions are taken from a previous experiment performed in SNL Hypersonic Wind Tunnel for the same cone geometry.[15] The freestream conditions are listed in Table 2.

Table 2: Simulation Parameters

Parameter	Value	Unit
M_∞	8.0	-
ρ_∞	0.024803	kg/m^3
p_∞	330.743	Pa
T_∞	44.9	K
T_o	620.0	K
T_w	279.0	K
γ	1.4	-
Pr	0.72	-
Re_∞/l	9584257	m^{-1}

IV. Results and Discussion

The DNS simulation begins by first computing the smooth cone meanflow for the case described in Table 2. From this result, LST is performed to determine the stability characteristics of the flow. These results in turn guide the design of the transition-delaying roughness element. A rough case meanflow is then computed with a single circumferential roughness element in place. With the converged meanflows, unsteady simulations using the blowing-suction actuator are computed for both the smooth and rough cases. An FFT analysis of the unsteady results is performed and the cases are compared.

A. Smooth cone meanflow results

Figures 3 and 4 contain the pressure and density contours from the meanflow simulation. As the simulation is axisymmetric, a single slice of the physical domain is presented. The domain is bounded at the top by the bow shock and below by the cone surface.

The pressure contours in Fig. 3 are typical of blunt cone results. As expected there is an increase in pressure across the shock with a significant increase near the stagnation point and a moderate pressure increase across the shock along the frustum.

Likewise, the density contours in Fig. 4 are also typical of blunt cone results. The density increases across the shock from the freestream as expected, with the highest contour values localized near the stagnation point. The other flow quantities, such as temperature and velocity are also typical of blunt cone results. The boundary layer profiles for performing LST analysis are taken from this meanflow simulation.

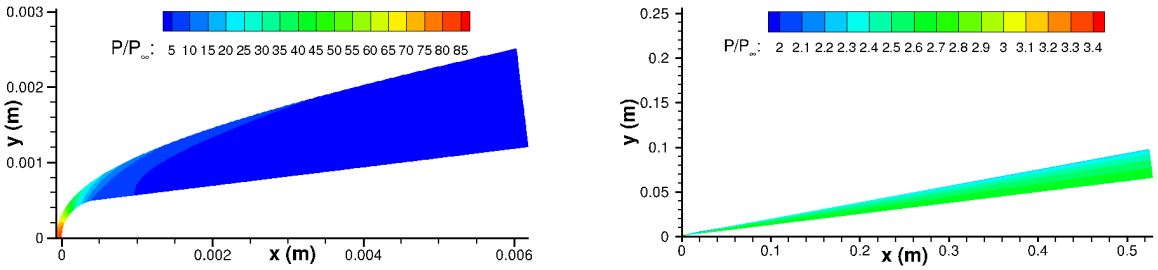

(a) (b)

Figure 3: Pressure contour behind bow shock over (a) the blunt nose and (b) cone frustum.

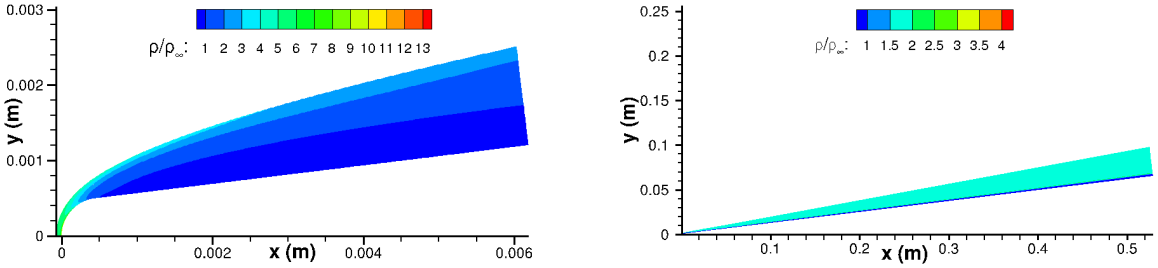

(a) (b)

Figure 4: Density contour behind bow shock over (a) the blunt nose and (b) cone frustum.

B. Stability analysis of meanflow and LST at 240 kHz

From the smooth cone meanflow data, an N-factor plot for mode S is computed. Using the empirical e^N method, disturbances in the boundary layer are measured by integrating the amplitude growth at a fixed frequency as the disturbance propagates downstream. The amplitude growth is found from LST using a steady parallel flow boundary layer profile, which is obtained from the meanflow data. The N-factor results are compared to experimental results to determine the frequency responsible for transition. The N-factor is defined below, where s is the distance along the surface, s_o is the first critical point, ω is the disturbance frequency and α_i is the growth rate.

$$N(\omega, s) = \int_{s_o}^{s} -\alpha_i ds \tag{17}$$

The N-factor plot in Fig. 5 below contains a frequency range from 180 to 400 kHz. Based on a previous experiment by Casper et. al.,[15,16] the intermittent turbulence results for the same cone geometry with the same Mach number and similar unit Reynolds number indicated that at 0.340 m, the instability wave intermittency began to drop as turbulent intermittency picked up. Comparing this 0.340 m location on Fig. 5 below, the location corresponds to an N-factor of 5.19 for a frequency of 240 kHz.

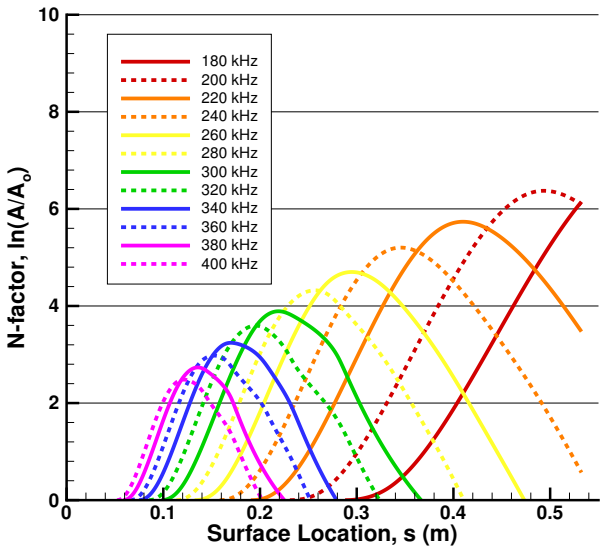

Figure 5: N-factor of mode S growth rate.

Taking 240 kHz as the mode S frequency most likely to cause turbulent transition, it can be targeted and suppressed using transition-delay roughness elements. This is done by locating the synchronization location—the point where the phase velocity of mode F crosses mode S—and placing a roughness element at that location or downstream of it. This approach of identifying the target frequency's synchronization location is the main idea behind Zhong's patented passive laminar flow control method.[5]

The phase velocity plot for the target frequency is given in Fig. 6 below. The point at which the modes cross could not be obtained directly from LST, which is known to occur, however, enough information was obtained to interpolate the synchronization location by connecting the ends of mode F and noting where it crosses mode S. A synchronization location of $s = 0.2436$ m along the cone surface was determined.

Along with the phase velocity, the growth rate for mode F and mode S at the target frequency is also determined. Figure 6 shows that mode S becomes unstable at $s = 0.1589$ m ($RF = 0.1737$) and becomes stable again at $s = 0.3452$ m ($RF = 0.2566$), meanwhile mode F remains entirely stable at the target frequency.

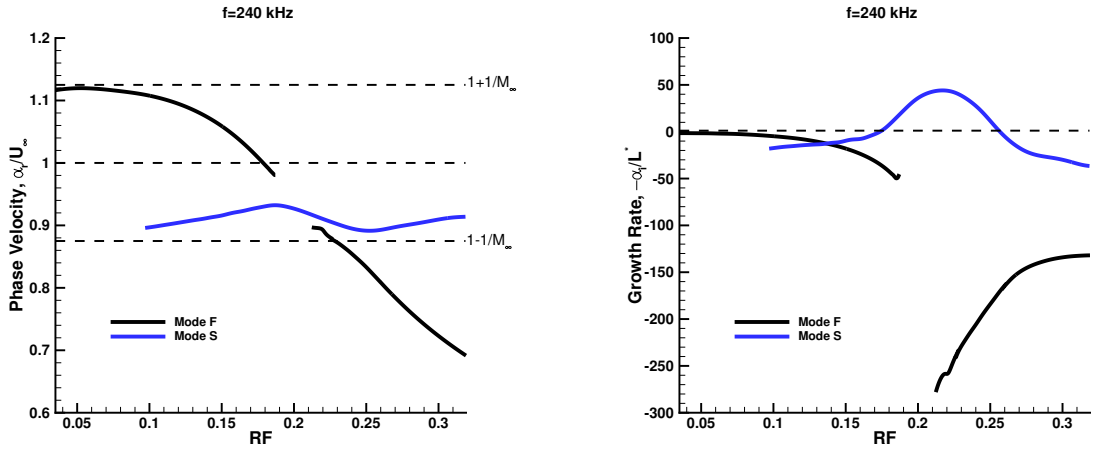

(a) (b)

Figure 6: (a) Phase velocity and (b) growth rate for mode F and mode S at 240 kHz.

It is well known that the second mode and higher modes are the acoustic instability waves in hypersonic boundary-layers,[17] and that mode S transitions from the first mode to the second mode after crossing mode F.[18] Hence, from Fig. 6 is it presumed that since all of the locations considered are downstream of the 240 kHz synchronization location, that the acoustic instability wave in question is the second mode. This presumption can be verified by examining the eigenfunctions at these locations. Figure 7, contains the pressure and temperature eigenfunctions for two locations: the synchronization location ($s = 0.2436$ m) and the experimental location where Casper et. al.[15] determined the turbulent intermittency begin to dominate ($s = 0.340$ m). The pressure eigenfunction for both locations are indicative of the second mode—comprising of one peak and one valley.[18] Moreover, the eigenfunctions have a negative growth rate and are consequently unstable. Thus, it has been shown that the instability wave considered in this simulation is the unstable second mode.

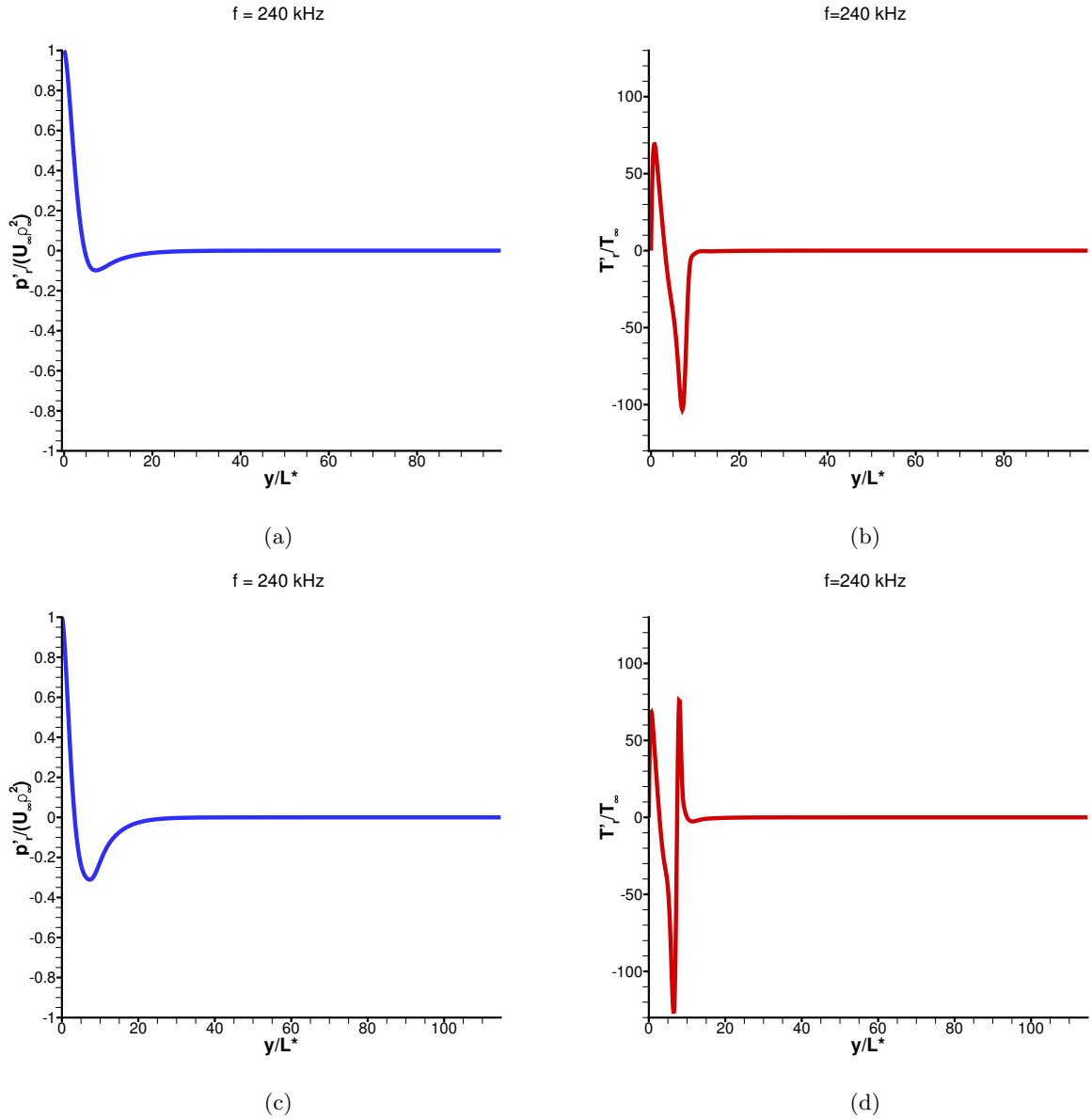

Figure 7: (a) Pressure and (b) temperature mode shapes at $s = 0.340m$ ($RF = 0.2541$). And (c) pressure and (d) temperature mode shapes at $s = 0.2436m$ ($RF = 0.2157$).

In addition to the N-factor analysis, a growth rate map of mode S for the majority of the smooth meanflow over a range of frequencies was constructed. From the map given in Fig. 8, the neutral curve can be viewed

alongside the peak unsteady growth rate. Within the confines of the neutral curve, the growth rates are unstable and those outside are stable. The peak unstable growth rate occurs around a frequency of 417 kHz, while the target frequency of 240 kHz and the frequencies most likely to lead to transition are quite lower. This is because the width of the neutral curve, for a given frequency, is wider for lower frequencies. As can be inferred from Eq. (17), one means of obtaining a large N-factor is for a given frequency to remain spatially unstable longer. Frequencies higher than 400 kHz were not considered in the the N-factor analysis, as they would have only produced smaller and smaller values of N and are not likely to lead to transition. Lastly, the neutral stability curve provides the range of relevant unstable second mode frequencies. Any unsteady pulse should contain the range of unstable second mode frequencies between 180 and 650 kHz. As seen in Fig. 2b, the pulse FFT nominally contains frequency content up to 1MHz, which is sufficient for covering the unsteady frequencies.

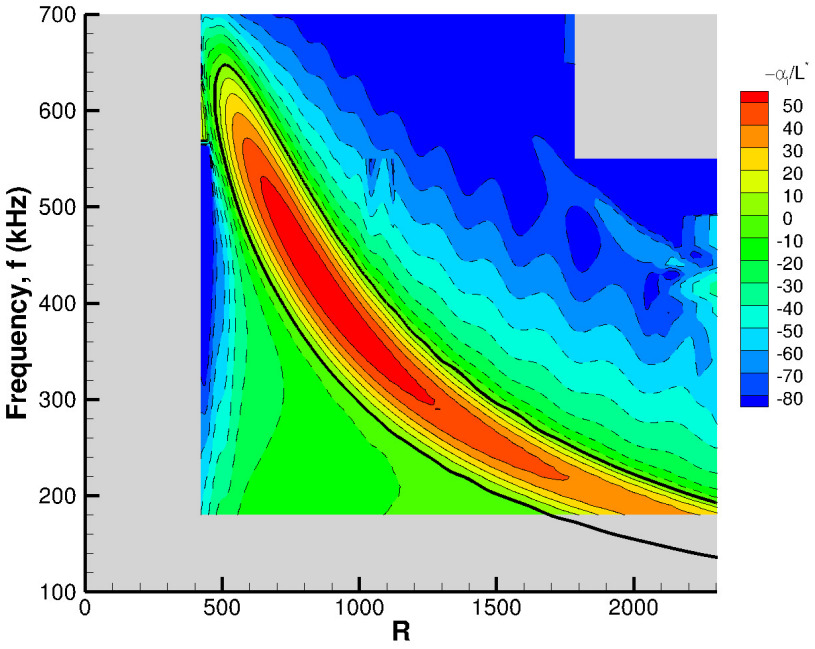

Figure 8: Growth rate map of mode S overlain with the neutral stability curve (▬). Solid contours (——) denote unstable growth rates, dashed contours (- - -) denote stable growth rates.

Lastly a note on Fig. 8 itself, the figure contains several gray spaces and artifacts. The gray area to the left of $R < 425$ was not computed since the closer the analysis gets to the blunt nose, the more the parallel flow assumption of LST is violated by the cone geometry. Moreover, the gray area below 180 kHz and in the upper right hand corner were not computed because the LST software could not track the mode S eigenvalue. Lastly, there are some artifacts within the map itself that are presumably caused when the software 'loses' the eigenvalue amongst the branches of the continuous spectrum before finding it again. In spite of these issues, the neutral curve and the space within it are well defined and free of artifacts.

C. Transition-delay roughness element design

Moving on to the design of the transition-delay roughness element; the location, height, and width of the element must be defined. In a previous computational/experimental collaboration, Fong et. al.[4] placed the element 5 cm downstream of the synchronization location. The rational for this was to guarantee the suppression of the target frequency. A parametric study by Fong et. al.[3] found that placing the roughness element at the synchronization location, suppressed frequencies higher than the target frequency while amplifying lower frequencies. Hence by placing the element further downstream, at essentially the synchronization location of a lower frequency, suppression of the target frequency was guaranteed. Moreover,

in the aforementioned computational/experiment collaboration, the height and width of the element were set to half the local boundary-layer thickness in height, and is twice the local boundary-layer thickness in width.

Following the convention set by Fong et. al.,[4] the surface location of the element is placed 5 cm downstream of the synchronization location at $s = 0.2936$ m. Figure 9 contains the boundary-layer profile at $s = 0.2936$ m extracted from the meanflow. The δ_{99} measure of the profile is used as the boundary-layer height. Table 3 contains the roughness element parameters.

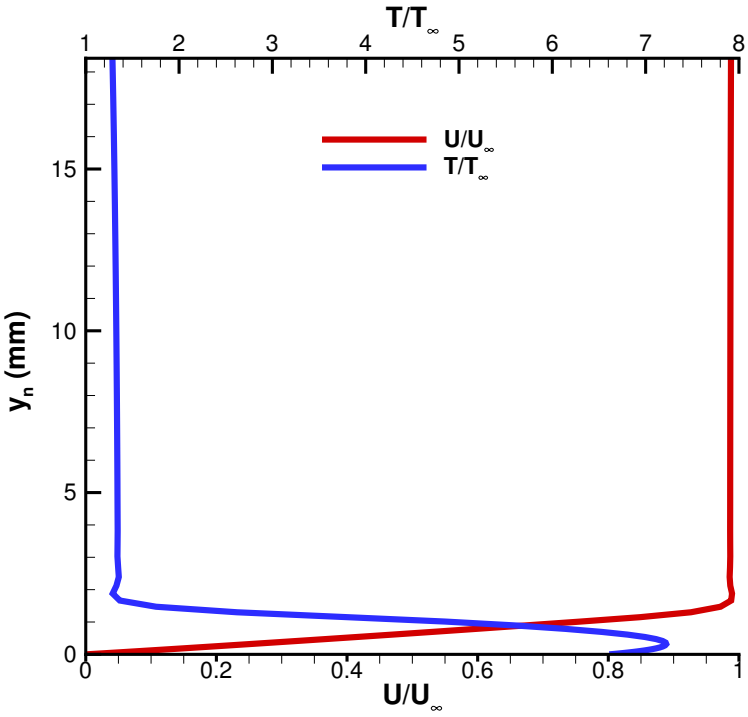

Figure 9: Velocity boundary-layer height at $s = 0.2936$

Table 3: Roughness Parameters

Parameter	Value	Unit
s	0.2936	m
δ_{99}	1.627	mm
h	0.8135	mm
w	3.254	mm

D. LST analysis at 218 kHz

Since the physical location of roughness element has been placed further downstream at $s = 0.2936$ it is only proper that some LST results be provided for this location. As mentioned previously, placing the roughness element downstream guarantees the suppression of the target frequency by essentially placing the element at the synchronization location of a lower frequency. Thus, we wish to determine the frequency whose synchronization location corresponds to $s = 0.2936$ m. After searching through a range of frequencies, 218 kHz provides a synchronization location closest to the roughness location. Figure 10 contains the phase velocity and growth rate plots for this frequency. As with the phase velocity plot in Fig. 6, the point where mode F and mode S cross could not be obtained directly from LST. Thus the synchronization location was determined by interpolating between the ends of mode F.

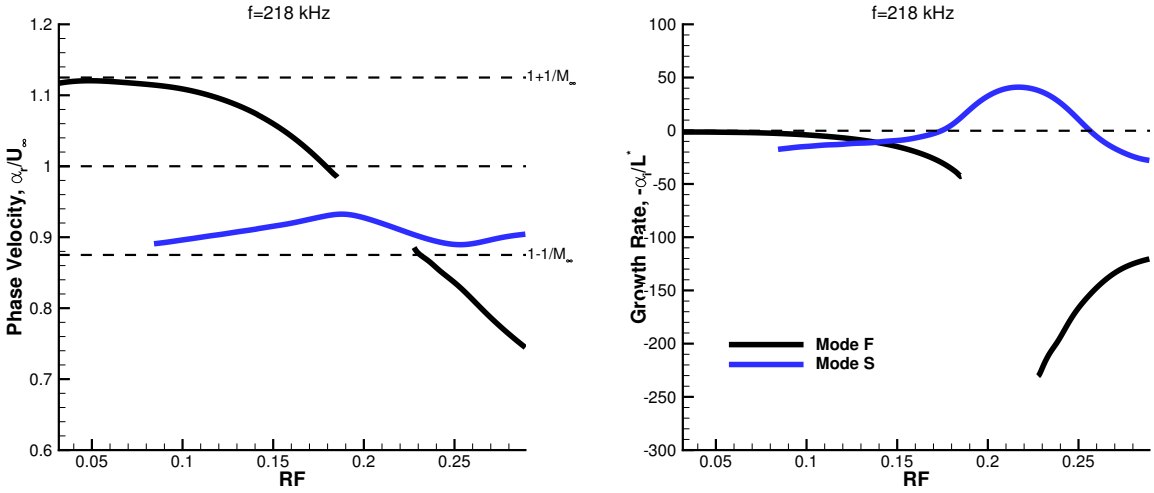

(a) (b)

Figure 10: (a) Phase velocity and (b) growth rate for mode F and mode S at 218 kHz.

E. Rough cone meanflow results

With the element dimensions defined, the rough case meanflow can be computed. Figures 11 and 12 provide an overall view of the meanflow pressure contour for the surface and the flow cross-section. This meanflow computation is an intermediate result in obtaining the full unsteady roughness simulation. But because the roughness introduces significant non-parallel flow in the vicinity of the roughness, LST analysis on this meanflow is not possible. Thus phase velocity plots and growth rate plots cannot be constructed, but that does not mean the rough meanflow is not without significant features.

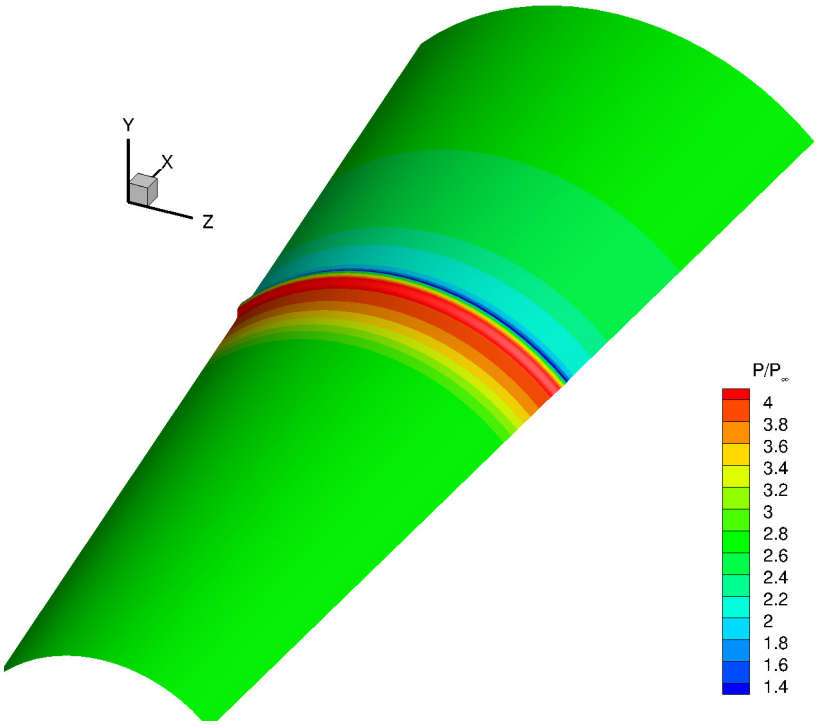

Figure 11: Meanflow pressure contours on cone surface.

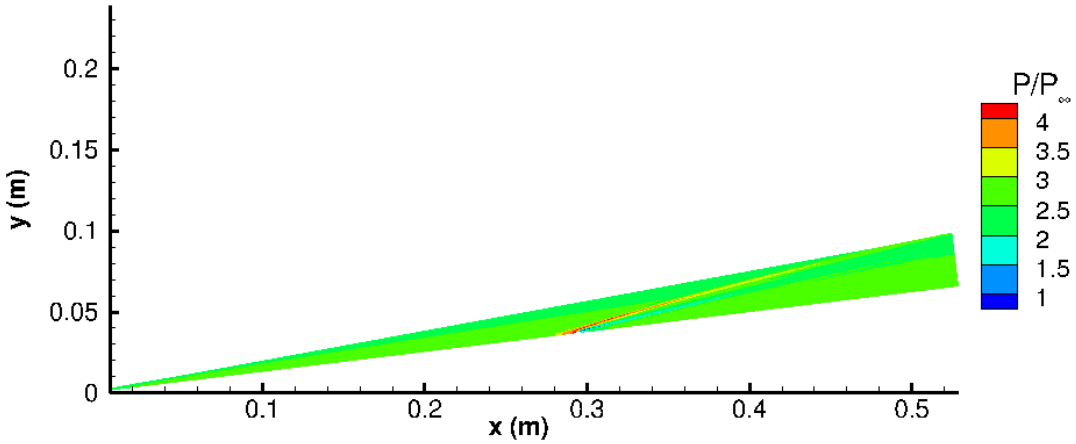

Figure 12: longitudinal cross-section of meanflow pressure contours.

The meanflow pressure contour plot nearest the element in Fig. 13 shows a Mach wave on the elements upstream edge with an expansion fan on the downstream edge. From this figure it can been seen that the presence of the element influences the upstream pressure field significantly by at least four element widths while the downstream pressure field shows less influence. This is a notable departure from flat plate simulations in which the influence of the element was felt nearly equally upstream and downstream.[2] The reason for the decreased downstream influence can be seen in the stream trace plot in Fig. 14. The downstream recirculation zone is not only smaller than in flat plate cases but is nearly nonexistent when compared to the extent of the upstream recirculation zone.

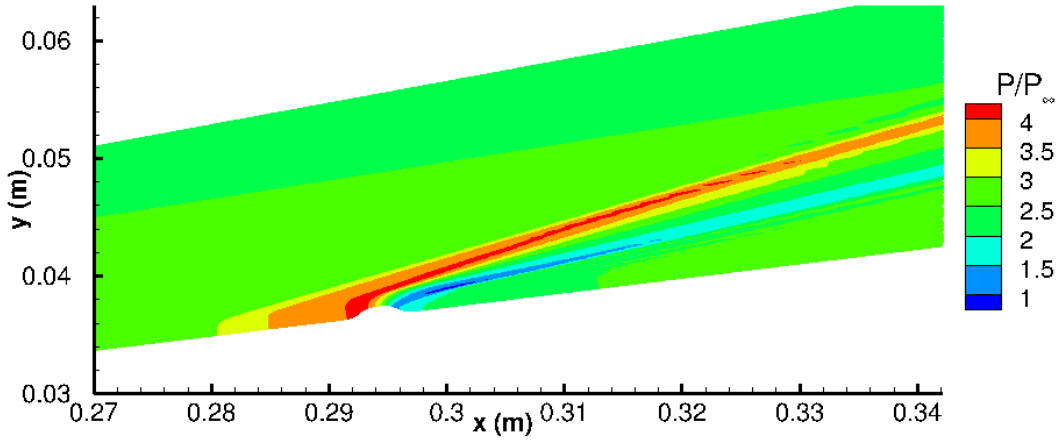

Figure 13: Meanflow pressure contours around roughness element.

The existence of the diminutive downstream separation zone is an interesting result, as it has been proposed by Tang et. al.[19] that it is this separation zone that is responsible for the second mode suppression via an application of Miles' Theory, in which the second mode undergoes amplitude reduction by reflecting off the zone. As will be seen later, despite the downstream separation zone's diminutive size, the roughness element is more than capable of suppressing its target frequency.

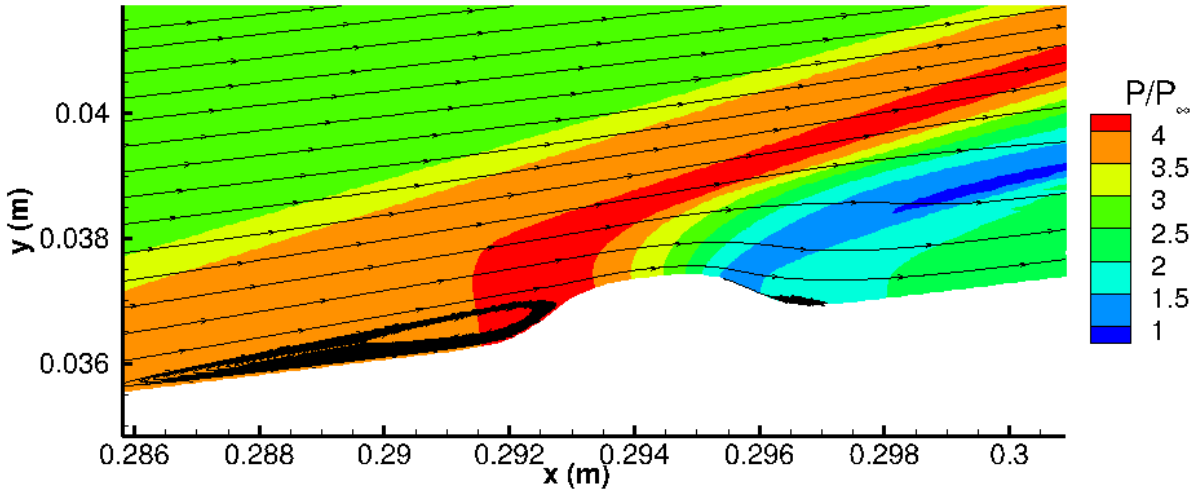

Figure 14: Stream trace around roughness element.

F. Unsteady results on a smooth cone

Moving forward from the meanflow simulations, a blowing-suction actuator is added to the smooth cone meanflow results and the pulse defined by Eq. (15) and Table 1 is imposed on the flow field. Figures 15 and 16 show the familiar second mode wave packet as it propagates downstream. As illustrated by Fig. 15, the unsteady results are axisymmetric. The blowing-suction actuator wraps circumferentially around the cone and thus produces a circumferential instability wave. Figure 16 shows the cross-sectional view of the instability wave. The surface location in the figure is in the vicinity of the element in the rough case and was chosen for better comparison with the roughness case.

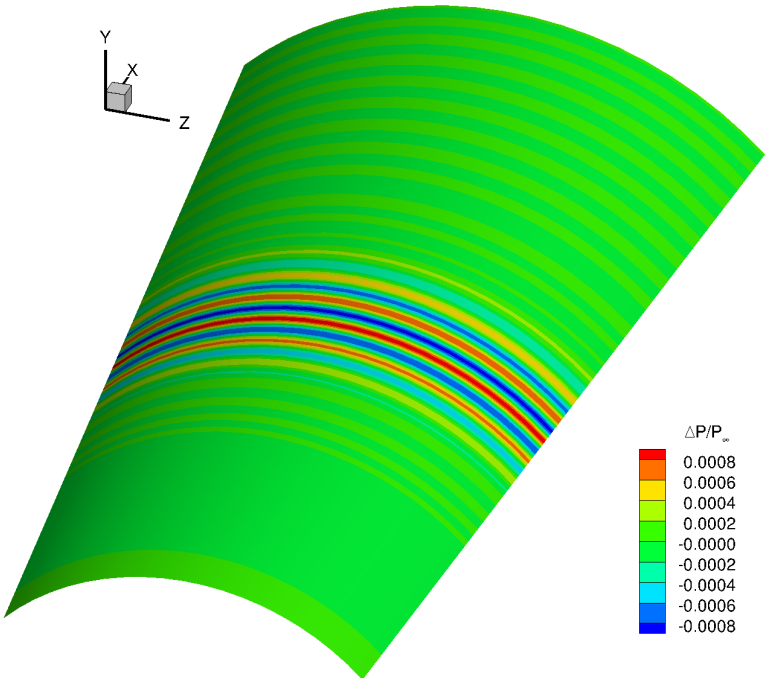

Figure 15: Surface view of second mode surface pressure perturbation on a section of cone frustum. The blowing suction actuator is located out of view at $s = 0.198$ m

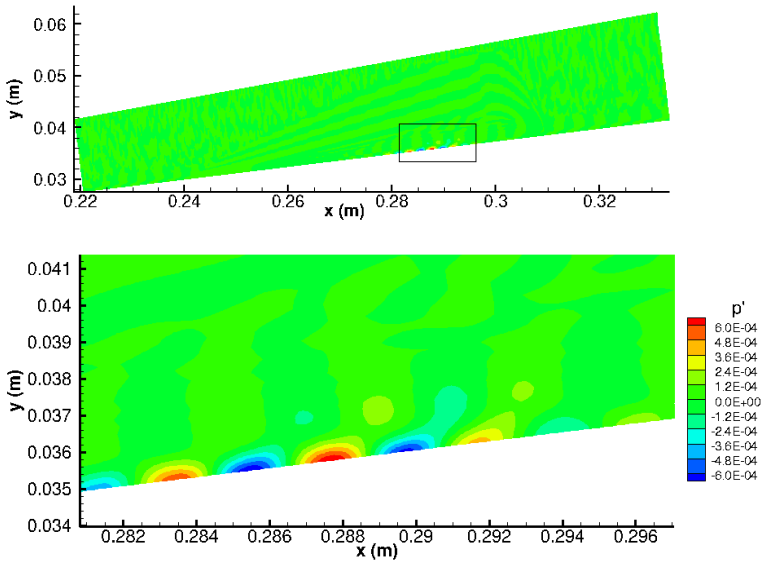

Figure 16: Pressure perturbation, p', of the second mode instability wave on a smooth cone.

In addition to the instantaneous view of the pressure perturbations provided in Fig. 16, the time history of the surface pressure perturbation can be extracted from the unsteady simulation. Figure 17 plots the instability wave for the smooth case at five separate locations over the same time period and the same pressure perturbation range. The figure highlights the instability waves constant wave speed and amplitude growth as it propagates downstream. The wave speed is calculated to be 1039 m/s, which is below the 1093 m/s of U_∞ but also above the 956 m/s of $U_\infty - a_\infty$, putting the wave speed in the slow acoustic range. Moreover, the waves amplitude grows 4.54 times over 8.1 cm, indicative of the unstable growth rate.

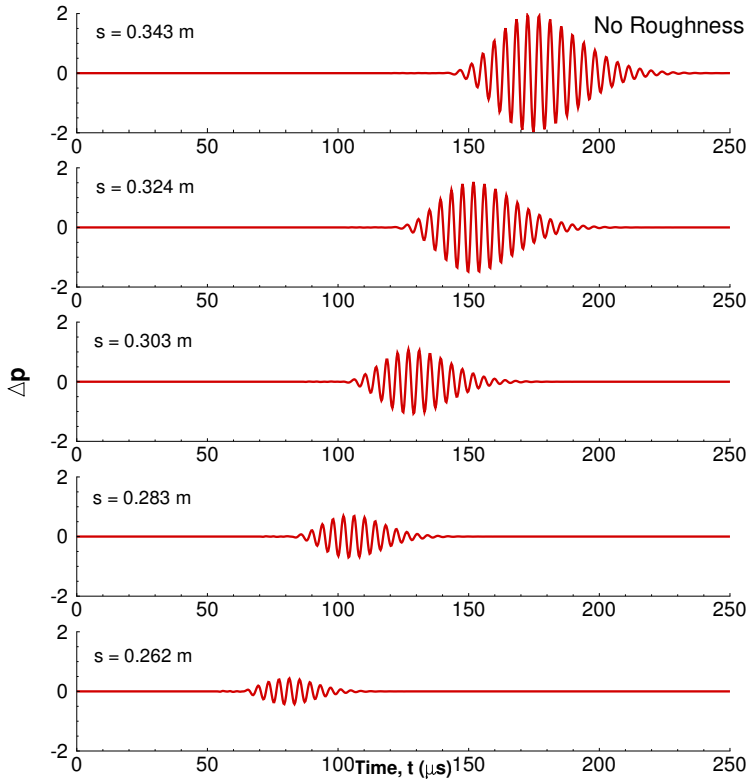

Figure 17: Time history of pressure perturbation at several surface locations on a smooth cone.

Fourier analysis of the time histories in Fig. 17 can provide insight into the amplitude growth of specific frequencies. Applying the transform to the entire surface produces the non-dimensional frequency spectrum map featured in Fig. 18. From the shape of the maps contours, it is clear that the instability waves frequency content changes as it propagates. Higher frequencies grow and then dampen out while lower frequencies, which initially have a background amplitude, eventually begin to grow at downstream locations. This brings to light that at any one location, only a narrow band of frequencies make up the instability, with the frequency content shifting to lower frequencies downstream.

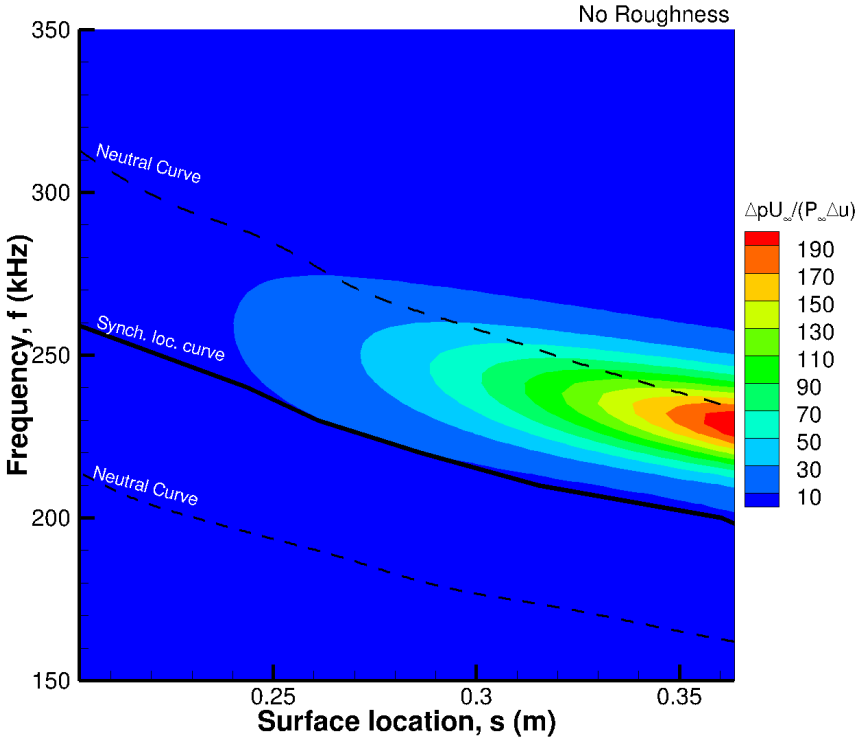

Figure 18: Non-dimensional frequency spectra of surface pressure perturbation along a smooth cone.

Overlaying the frequency spectrum in Fig. 18 are two sets of curves: the neutral curve and the synchronization location curve. The neutral curve is the same curve from Fig. 8. As expected the instability grows downstream of the first branch of the neutral curve. And close examination of the contour lines for a fixed frequency show that the pressure perturbation begins to dampen after crossing the second neutral curve branch as expected. The synchronization location curve depicts a handful of synchronization locations at fixed frequencies. As with synchronization locations described previously, the points were found by interpolating where mode F crosses mode S. An interesting and unexpected result is how well the curve follows the contour of the frequency spectrum. It would suggest that it is the interaction of the second mode with mode F that kick starts the growth of the instability wave. It should be noted that the appearance of the first contour at its most upstream location is probably due to the location of the blowing-suction actuator at $s = 0.198$ m. Presumably, if the actuator were moved farther upstream, and the domain of Fig. 18 included more of the cone surface, we would see the synchronization location curve track the upstream edge of the frequency spectrum.

Lastly, Figs. 19 and 20 contain select FFT results for fixed frequency and fixed location from the frequency spectrum. For fixed frequency, Fig. 19 looks at a range that covers the whole of the instability including the target frequency of 240 kHz. As already noted, the higher frequencies tend to grow and then dampen out, this can be seen for the frequencies of 270, 260, 250 and 240 kHz. Moreover, the lower frequencies, such as 210, 220 and 230 kHz, start low and eventually grow at downstream locations. Notably, the location where the spatial evolution reaches its maximum corresponds to the second branch of the neutral stability curve.

Figure 20 looks at four fixed locations: the synchronization location for the target frequency (0.243 m),

0.268 m, the roughness location (0.293 m) and where the experimental turbulent intermittency begins to dominate (0.340 m). As noted previously, for any given location, the prevailing instability frequencies consist of a narrow band. Moreover, the peak amplitude of this narrow band increases downstream. More subtly, however, the frequency of the peak decreases moving downstream.

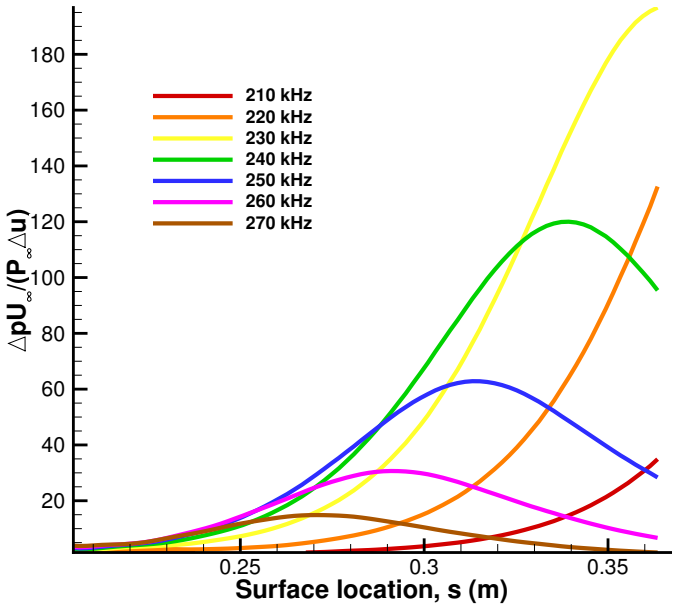

Figure 19: Spatial evolution of fixed frequency FFT results for smooth case.

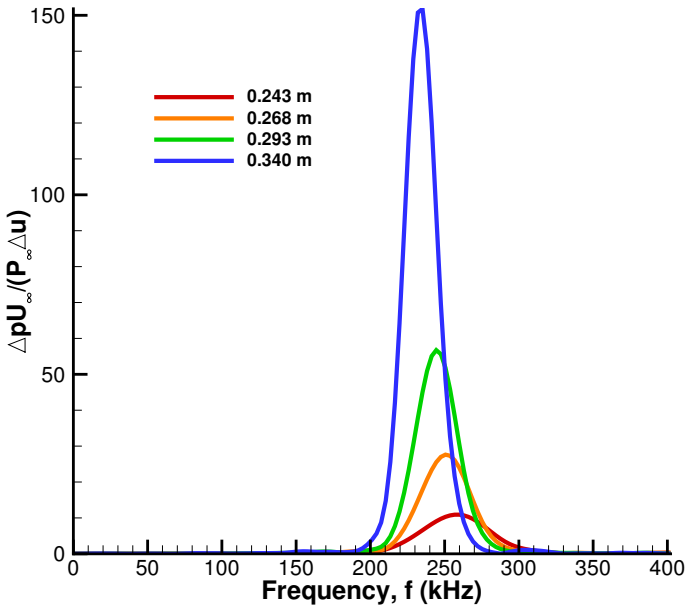

Figure 20: Fixed location frequency spectrum for a smooth case.

G. Unsteady results on a rough cone

Just as with the smooth cone meanflow, a blowing-suction actuator is added to the rough cone meanflow and a pulse is imposed on the flow field. Figure 21 shows an overview of the second mode as it propagates downstream toward the roughness element.

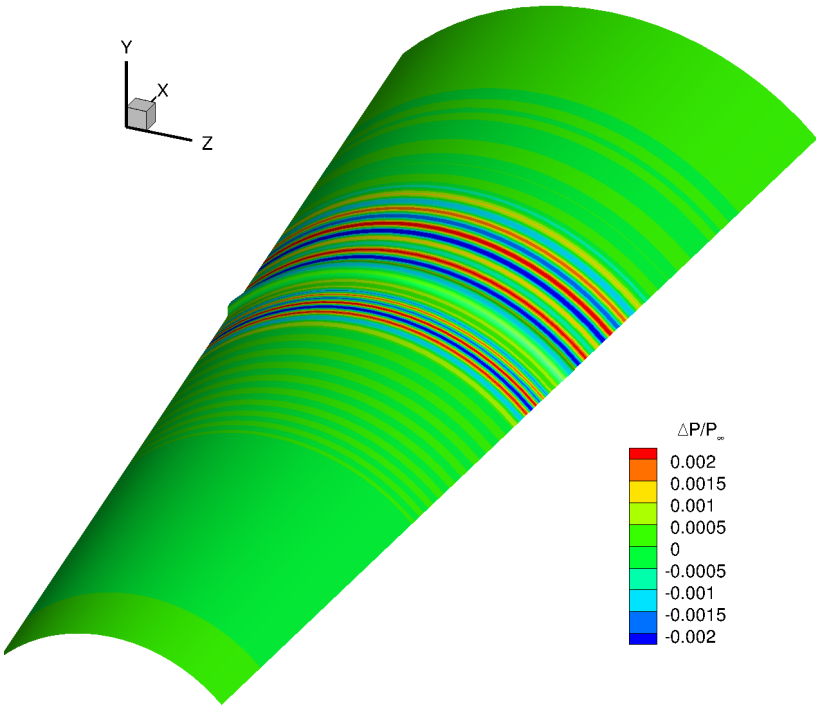

Figure 21: Surface view of second mode surface pressure perturbation on a section of cone frustum. The blowing suction actuator is located out of view at $s = 0.198$ m.

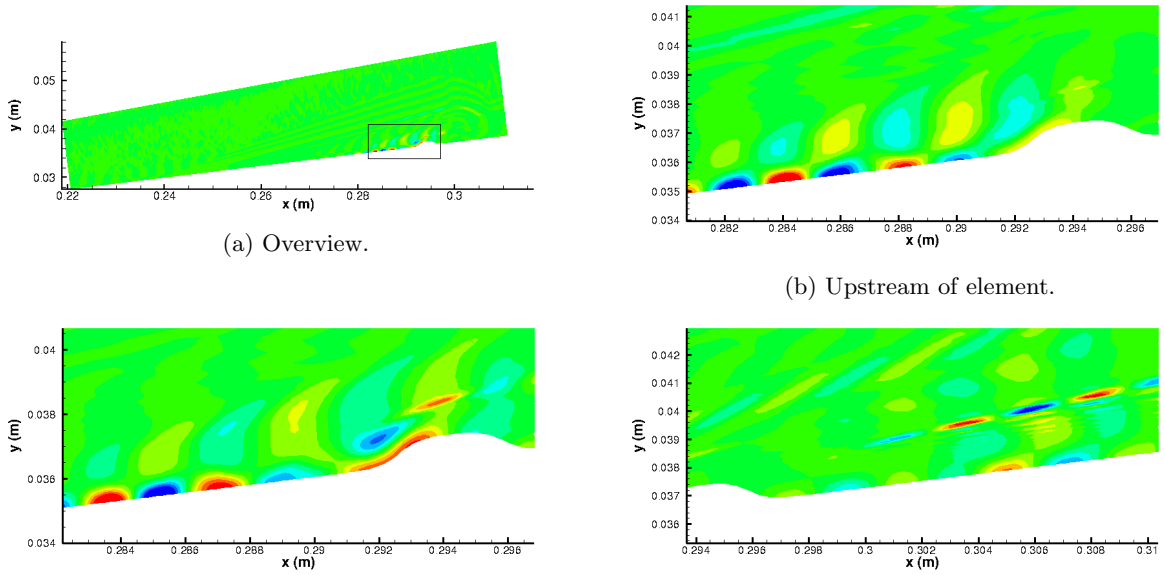

(a) Overview.

(b) Upstream of element.

(c) Traveling over element.

(d) Downstream of element.

Figure 22: Rough case cross-sectional view of second mode pressure perturbation.

Figure 22 features the second mode pressure perturbations at several instances: once when the disturbance is upstream of the element, another when it is passing over the element, and lastly when it is downstream of the element. Comparing Fig. 22b with Fig. 16 shows a much stronger disturbance in the rough case than in the smooth case. This is consistent with previous flat plate simulations in which the trend is to amplify the disturbance frequency band immediately upstream of the element before suppressing the desired range.[3] In Fig. 22c, the disturbance is stretched and deformed as it passes over the element. On close examination the weaker pressure perturbation seen above the main perturbation would appear to grow in amplitude as the wave packet negotiates the slope of the element. These newly amplified perturbations dampen out quickly; disappearing just as they pass over the element. They should not be confused with the strong off-the-wall perturbations seen in Fig. 22d, which are 'shed' from the main disturbance as it passes down the backside of the element and carried away in the expansion fan. These 'shed' features notwithstanding, the most important feature of Fig. 22d is the significant suppression of the second mode on the wall when compared to the incoming second mode in Fig. 22b.

Just as in the smooth case results, the time history of the surface pressure perturbation can be extracted from the unsteady simulation. Figure 23 plots the time history at five separate locations. The plots share the same domain and range as the plots in Fig. 17 for ease of comparison. The figure shows that the disturbance grows considerably between the first two locations, dampens after passing the roughness location ($s = 0.2936$ m), and then proceeds to grow again. Examined more closely, between $s = 0.262$ m and $s = 0.283$ m the perturbation amplitude grows 139% over 2.1 cm. Between $s = 0.283$ m and $s = 0.303$ m, the disturbance passes over the roughness element which in turn suppresses the packets amplitude by 57%. From this new state, the perturbation amplitude grows 150% between $s = 0.303$ m and $s = 0.343$ m. This amounts in a total amplitude growth of 159% over the span of 8.1 cm.

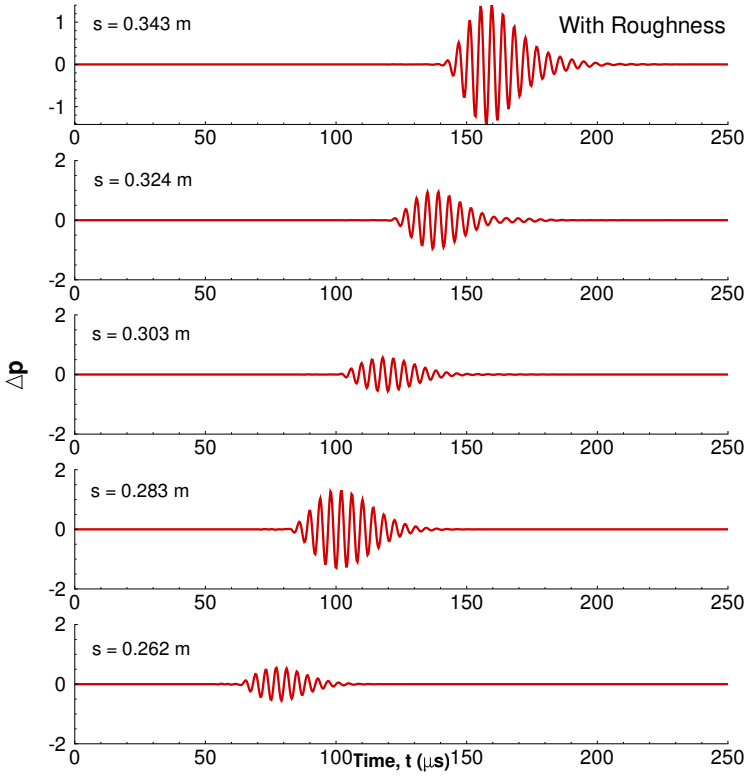

Figure 23: Time trace of pressure perturbation at several surface locations on a cone with a finite roughness element.

Comparing the last location ($s = 0.343$ m) between Figs. 17 and 23, the disturbance packet in the rough case is 39% times smaller than in the smooth case. The same reduction in magnitude can also be noted for the $s = 0.303$ m and 0.324 m locations as well. Comparison of the time histories between the two cases illustrates quite clearly the surface elements ability to suppress the second mode. It should be

noted, however, that the roughness element does not, in actuality, stabilize the second mode. For all intents and purposes the growth rate remains unstable, as seen by its amplification before and downstream of the roughness. It is only in the vicinity of the element that its amplitude is reduced. Previous discourse on this topic has left the impression that surface elements stabilize the flow downstream of the element. This is why in the experimental undertakings of this topic, successive roughness strips have been employed to delay transition.

Moving on to the Fourier analysis of the time histories, Fig. 24 is the non-dimensional frequency spectrum map of the rough case. As in the smooth case, the map is overlaid with the neutral curve and synchronization location curve. These curves come from the stability analysis done on the smooth cone. Due to the non-parallel flow in the vicinity of the roughness, stability analysis using LST is not valid. Thus, the curves serve to compare how the unsteady flow with roughness differs from the nominal case. The most notable feature of the spectrum are the contour wiggles in the vicinity of the roughness element denoted by the red line. It would appear the surface perturbation enters an irregular state in which the perturbation spreads and contracts to higher and lower frequencies, all the while undergoing an overall reduction. Aside from this prominent feature, the general shape of the contours is reminiscent of the smooth case with some distinct differences. The first is the magnitude of the contours; both Figs. 24 and 18 share the same contour scaling. Notably, the case with roughness is less amplified, never reaching the same peak amplitude. Another difference is the growth of frequencies below the synchronization curve. This growth below the synchronization curve, however, suggests that the range of frequencies that can undergo growth is not bounded as is implied by the smooth case in Fig. 18. More downstream results are needed to support this speculation however and to determine its significance.

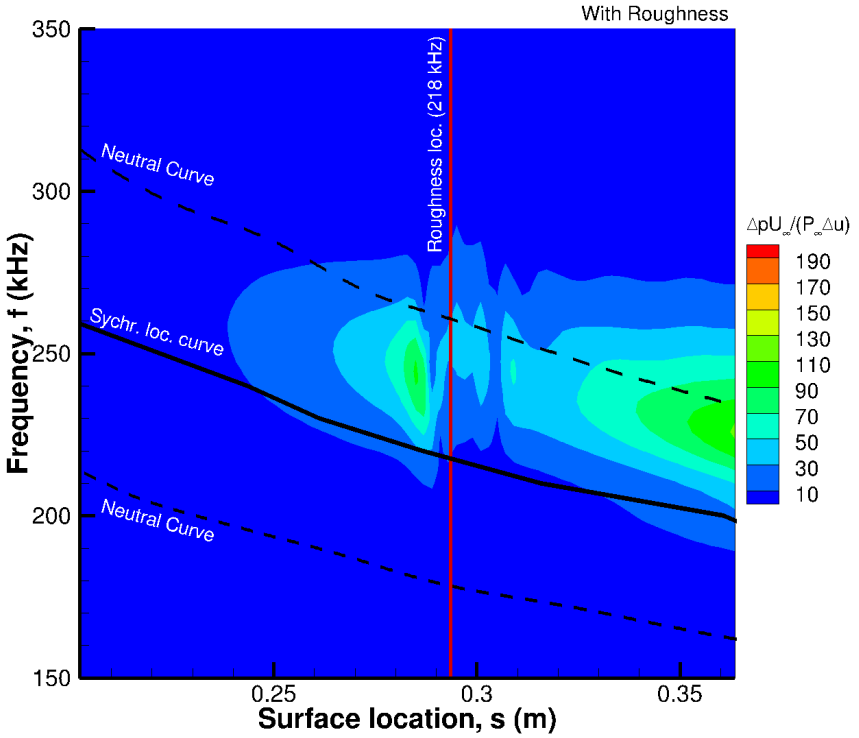

Figure 24: FFT map with neutral curve and the synchronization location of multiple frequencies.

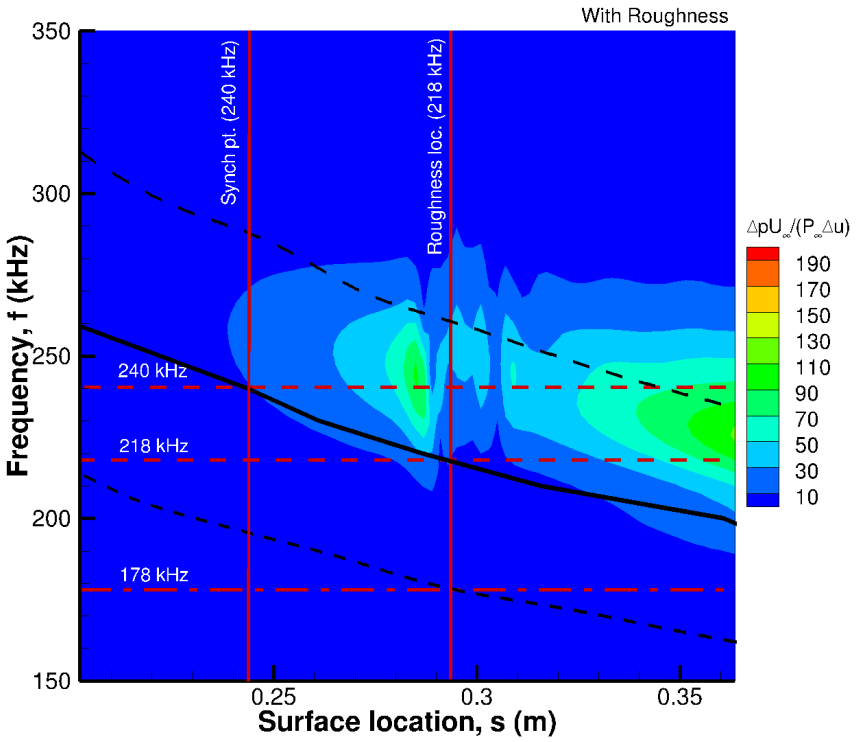

Figure 25: FFT map with neutral curve and the synchronization location of multiple frequencies.

In addition to Fig. 24, Fig. 25 is the same contour plot but with lines denoting features important to this paper. The first is the vertical line denoting the synchronization location for the target frequency of 240 kHz. As the N-factor and LST analysis showed, 240 kHz was determined to be the first frequency responsible for causing transition. As expected the dashed line denoting 240 kHz intersects the vertical line on the synchronization curve. Further down this horizontal line we see an overall suppression of the 240 kHz frequency, which is very apparent in Fig. 26 and is the desired outcome of the roughness design. Moreover, at this intersection point of synchronization location and target frequency is also the first place where we see frequency growth below the synchronization curve. Also in featured in Fig. 25 is the roughness location and its synchronization frequency. For this frequency of 218 kHz there is marginal suppression but more importantly frequencies lower than it start to amplify downstream. The last horizontal line in the figure is the dash-dot line at 178 kHz, which denotes the first neutral point at the roughness location. There has been some argument and speculation that it is the neutral point with respect to the roughness location that dictates which frequencies are suppressed or amplified. But as the frequency spectrum shows, there is both growth and suppression at frequencies greater than the neutral point frequency. And as seen in the figure, the first branch of the neutral curve is generally far removed from the observed frequency response.

Lastly, Figs. 26 and 27 contain FFT results for fixed frequency and fixed location. For fixed frequency, Fig. 26 looks at the same range considered in the smooth case plotted over the same range and domain. But unlike the smooth case there is obvious suppression especially for 240 kHz and higher and moderate suppression for 230 and 220 kHz. There is however some growth for 210 kHz not seen in the smooth case. This growth is expected as the frequency is lower than the roughness synchronization location frequency of 218 kHz. If the unsteady simulation were extended downstream we would expect to see more growth of frequencies below 218 kHz. Also evident is the disturbance amplification upstream of the roughness element, which is consistent with flat plate simulations.

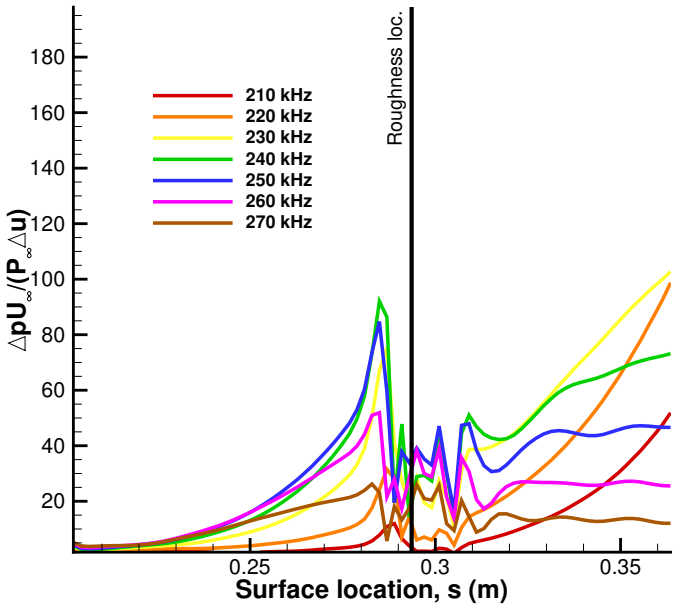

Figure 26: Spatial evolution of wall pressure perturbation at fixed frequency FFT results for a rough cone.

Figure 27 also looks at the same four fixed location considered in the smooth case. Here, again the suppression of the narrow band of frequencies is obvious. There is some amplification of the 0.268 m band but not so much as to dominate the already suppressed bands. In the next section the rough and smooth cases will be compared and contrasted more closely with more definitive conclusions on the effect of roughness on this cone.

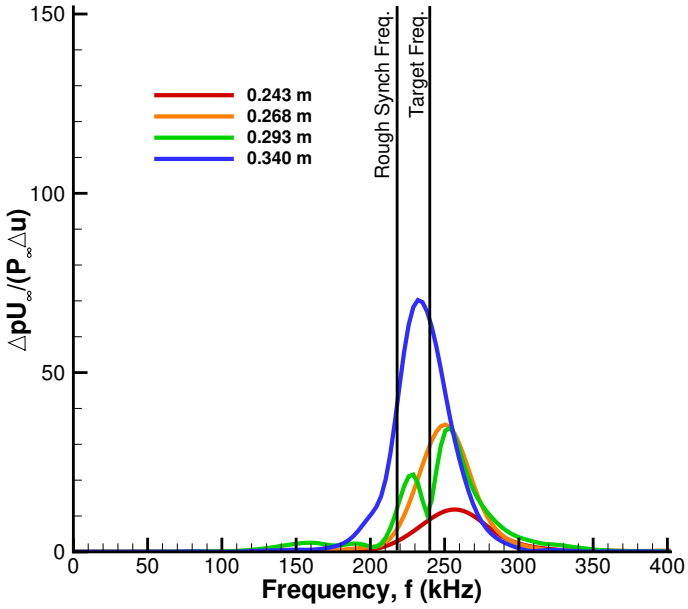

Figure 27: Fixed location frequency spectrum results for a smooth cone.

H. Comparison of smooth and rough case FFT results

For a clearer understanding of the effect of transition-delaying roughness, the frequency spectrum results for both the smooth and rough cases are reproduced here side-by-side. Figure 28 contains both frequency spectrum maps with letters in different region denoting important features. The first region is A, which denotes an area upstream of the roughness in which the frequency is higher than the local synchronization frequency. Between the smooth cone contour on the left and rough contour on the right, there is a mild overall amplification of all frequencies before reaching the roughness. Moving downstream, region B is entered. This region denotes an area where frequencies are suppressed significantly. It is this behavior which promotes surface roughness as an approach to passive transition-delay. Moving onto regions below the synchronization curve, region C sees some amplification between the smooth and rough case. This behavior may not be as notable however since it is consistent with the amplitude growth in region A. Some of the frequencies in region C, being above the roughness synchronization frequency, will be suppressed while the others will be amplified. This brings us to region D in which frequencies previously unamplified are amplified. This behavior can be detrimental to the passive transition-delay approach as these amplified frequencies can lead to transition on their own, but can be resolved easily by using successive roughness strips.[4]

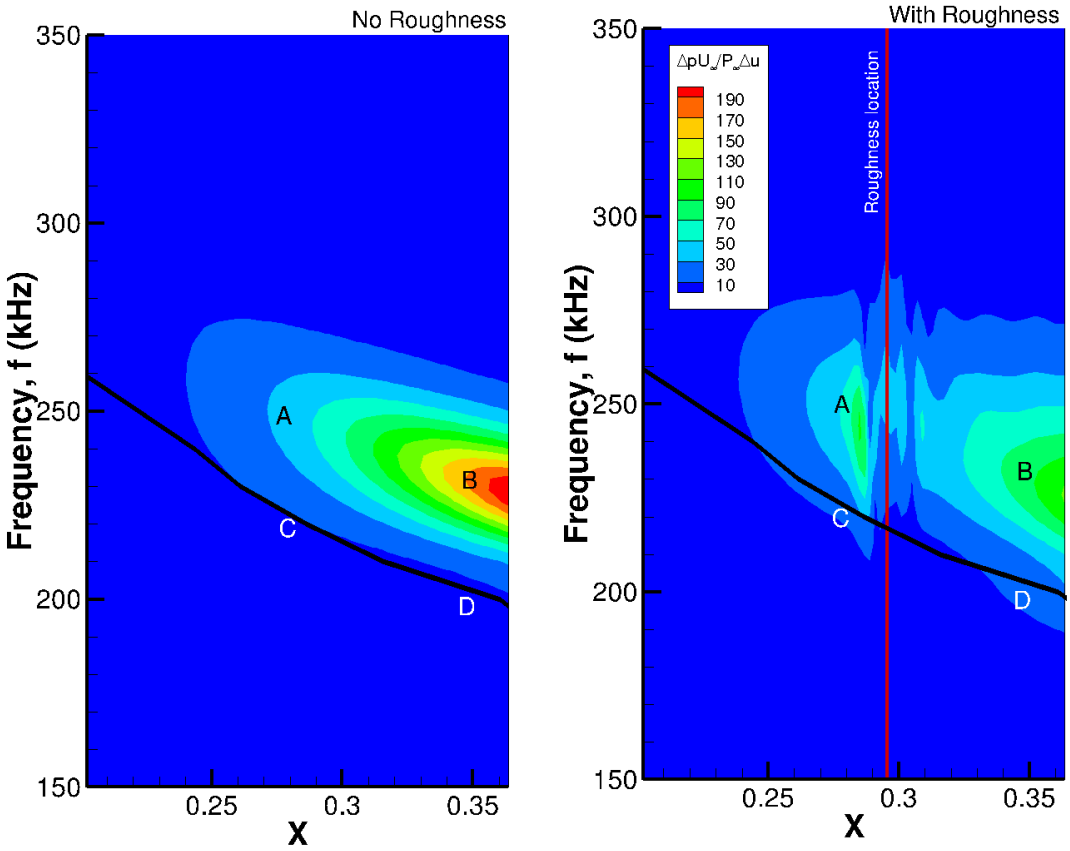

Figure 28: Comparison of FFT maps for both instances of the smooth and rough cases.

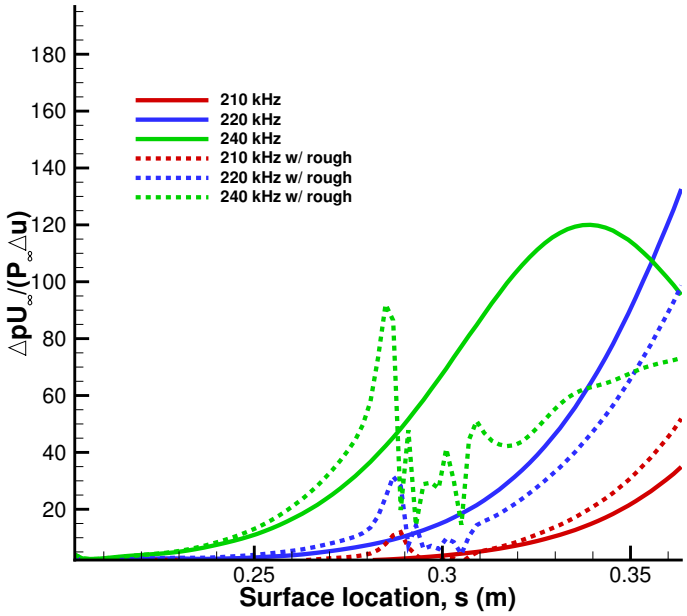

(a)

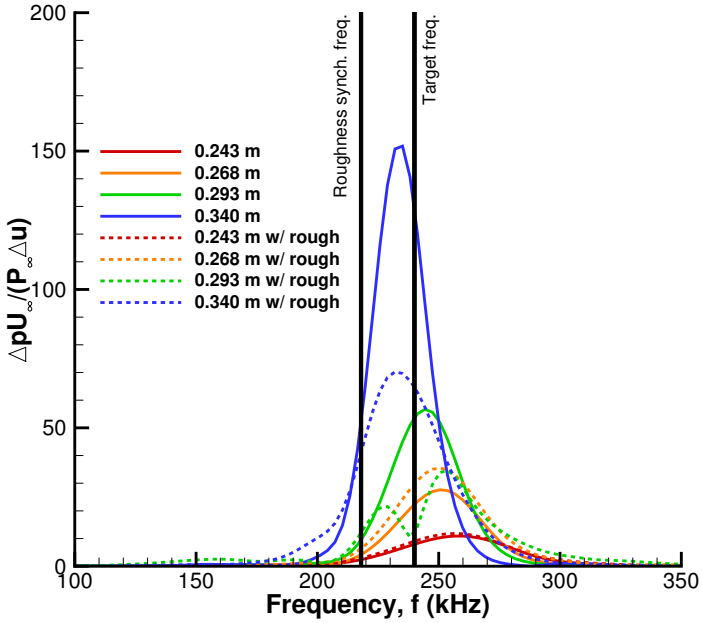

(b)

Figure 29: Comparison of FFT results for smooth and rough cases

Lastly, the results for fixed frequency and fixed location are compared together. Figure 29a compares several fixed frequencies in which the frequencies chosen are the target frequency (240 kHz), a frequency below the target frequency (220 kHz) but above the roughness synchronization frequency, and a frequency below the roughness synchronization frequency (210 kHz). For 240 kHz the instability is significantly suppressed

by the roughness. For 220 kHz the instability is mildly suppressed by the roughness, which is to be expected since the frequency is only slightly higher than the roughness synchronization location frequency. And lastly, for 210 kHz the instability is slightly amplified by the roughness since its frequency is below the roughness synchronization location frequency. Note that these last two results bound the synchronization location frequency of 218 kHz, show the intended suppression/amplifying behavior, and differ by only 10 kHz. This is indicative of the precision to which the passive laminar flow control method can be applied. In hindsight, it may not have been necessary to follow Fong's convention of placing the roughness element 5 cm downstream in order to guarantee suppression of the 240 kHz frequency—in future applications this step may be omitted.

Moreover, Fig. 29b compares several fixed locations of the frequency spectrum. At $s = 0.243$ m, the synchronization location of the target frequency, there is only the slightest amplification across the entire band. This is not surprising since the location is upstream of the roughness element. The next location at $s = 0.268$ m is also upstream of the roughness and here too the frequency band is amplified. From peak to peak the amplification is 28%. The next location at $s = 0.293$ m is at the roughness location, here there is clear suppression and some modulation of the band. From peak to peak the suppression here is nearly 40%. And lastly at $s = 0.340$ m, the experimental location where turbulent intermittency begins to dominate, there is a peak-to-peak suppression of 54%. An interesting observation of this comparison plot is slight growth of frequencies greater than 260 kHz for $s = 0.293$ m. This higher frequency growth is not apparent at $s = 0.340$ m in which the amplified frequencies are below 215 kHz. This growth above 260 kHz at $s = 0.293$ m may be due to the proximity of the roughness element.

V. Summary

This paper presents a newly developed DNS code to explore the effect of isolated surface roughness on the transition process on a hypersonic cone. The code solves the three-dimensional Navier-Stokes equations under a perfect gas assumption. The axisymmetric roughness element is replicated using a body-fitted grid over an analytical shape. This approach along with shock-fitting allows for a uniform 5^{th}-order global accuracy throughout the domain. Unsteady results are produced using a blowing-suction actuator, which introduces a Gaussian pulse to stimulate the second mode instability.

This is the first time transition-delay roughness has been simulated on a blunt cone. Previous computational investigations of transition-delay roughness are limited to flat plate simulations. Moreover, previous simulations of roughness on a cone were not investigating transition-delay roughness, were not using higher order methods, or using simulations that did not include the effect of the bow shock in their simulations. The ability for this code to combine high-order finite-difference methods with shock-fitting in order to simulate transition-delay roughness is what makes this code unique.

The new code is then put to work investigating the finite roughness effect on modal growth of a Mach 8 blunt cone. The method patented by Zhong for hypersonic laminar flow control is used to identify the frequency likely to lead to transition.[5] This entails computing the meanflow's N-factor for a range of frequencies, identifying the target frequency, finding its synchronization location and then designing a roughness-element to delay transition.

The findings of the simulation are consistent with the findings of Fong and Zhong[2–4] for a hypersonic flat plate. Before this cone simulation, there was no guarantee that what is true for the synchronization location hypothesis in a planer flow is true in a conical flow. The findings in this paper reinforce and role the synchronization location plays in suppressing the second-mode instability with roughness—mainly, that roughness elements shorter than the local boundary layer height can suppress frequencies within the instability wave bandwidth. Moreover, the roughness suppresses frequencies above the synchronization frequency of the roughness location, while amplifying those below it. The findings also show that without additional roughness elements placed downstream, the suppressed frequencies will continue to grow.

One instance, however, in which the cone simulation differs remarkably from flat plate simulations is the downstream separation zone behind the roughness: the separation zone is significantly smaller for the cone. The reason for this was not extensively investigated but could be because the cone is axisymmetric. But the reason this result is curious is because the downstream separation zone has been suggested as a damping mechanism. The mechanism posits that a vortex sheet between the separation zone and the rest of the boundary layer prevents the second mode from penetrating into the zone, thus reflecting it back in to the boundary layer towards the sonic line.[19] This reflection incurs an amplitude reduction via Miles' law, thus suppressing the second mode. This may be all well and true, however the extent of the vortex sheet

downstream would suggest that the amount of damping is dependent on the size of the separation zone. Thus with a diminutive separation zone, minimal suppression would be expected, which is not the case in this simulation. Instead, the suppression of the second mode on a cone is comparable with the suppression of a flat plate. Again the diminutive separation zone is only a cursory observation but its role as a suppression mechanism has merit and deserves further investigation.

Future work on this data set will include extending the frequency spectrum map over the entire cone length—the purpose of which is to better evaluate the correlation between the synchronization location curve and evolution of the instability bandwidth for both smooth and rough cases. Furthermore, an additional data set will explore successive roughness strips placed downstream, with the purpose of suppressing all transition causing frequency growth. This effort is part of the computational/experimental collaboration with Dr. Casper, an effort that will hopefully further validate our simulation approach and lead to new ideas on transition-delaying roughness. And lastly, and heretofore unmentioned, is the new DNS code capability of simulating discrete 3-D isolated roughness in much the same manner as the axisymmetric roughness previously described. To this point, only 2-D and axisymmetric simulations of transition-delay roughness have been explored, the next logical step is expand the simulations to include 3-D isolated roughness.

Acknowledgements

This work is sponsored by the Air Force Office of Scientific Research, USAF, under AFOSR Grants #FA9550-15-1-0268, monitored by Dr. Ivett Leyva. The computations are mainly run on XSEDE resources provided by Texas Advanced Computing Center (TACC) and San Diego Supercomputer Center (SDSC) under grant number TG-ASC090076 supported by National Science Foundation. The views and conclusions contained herein are those of the author and should not be interpreted as necessarily representing the official policies or endorsements either expressed or implied, of the Air Force Office of Scientific Research or the U.S. Government. Dr. Katya Casper is acknowledged for her collaboration and agreeing to run roughness experiments, validative, explorative or otherwise, in Sandia National Labs Hypersonic Wind Tunnel facility.

References

[1]Schneider, S. P., "Summary of Hypersonic Boundary-Layer Transition Experiments on Blunt Bodies with Roughness," *Journal of Spacecraft and Rockets*, Vol. 45, No. 6, 2008, pp. 1090–1105.

[2]Fong, K. D., Wang, X., and Zhong, X., "Numerical simulation of roughness effect on the stability of a hypersonic boundary layer," *Computers and Fluids*, Vol. 96, 2014, pp. 350–367.

[3]Fong, K. D., Wang, X., and Zhong, X., "Stabilization of hypersonic boundary layer waves using 2-D surface roughness," *43rd Fluid Dynamics Conference*, January, 2013, pp. 1–20.

[4]Fong, K. D., Wang, X., Huang, Y., Zhong, X., McKiernan, G. R., Fisher, R. A., and Schneider, S. P., "Second Mode Suppression in Hypersonic Boundary Layer by Roughness: Design and Experiments," *AIAA J.*, Vol. 53, No. 10, 2015, pp. 1–6.

[5]Zhong, X., Fong, K. D., and Wang, X., "Hypersonic laminar flow control," 2014.

[6]James, C. S., "Boundary-Layer Transition on Hollow Cylinders in Supersonic Free Flight as Affected by Mach Number and a Screwthread type of Surface Roughness," Tech. Rep., 1959.

[7]Holloway, P. F. and Sterrett, J. R., "Effect of Controlled Surface Roughness on Boundary Layer Transition and Heat Transfer at Mach Numbers of 4.8 and 6.0," *Nasa Tn D-2054*, April, 1964.

[8]Fujii, K., "Experiment of the Two-Dimensional Roughness Effect on Hypersonic Boundary-Layer Transition," *Journal of Spacecraft and Rockets*, Vol. 43, No. 4, 2006, pp. 731–738.

[9]Chynoweth, B. C., Ward, C. A. C., Greenwood, R. T., McKiernan, G. R., Fisher, R. A., and Schneider, S. P., "Measuring Transition and Instabilities in a Mach 6 Hypersonic Quiet Wind Tunnel," *44th AIAA Fluid Dynamics Conference*, January, 2014.

[10]Zhong, X., "High-Order Finite-Difference Schemes for Numerical Simulation of Hypersonic Boundary-Layer Transition," *Journal of Computational Physics*, Vol. 144, No. 2, 1998, pp. 662–709.

[11]Huang, Y. and Zhong, X., "Numerical Study of Hypersonic Boundary-Layer Receptivity with Freestream Hotspot Perturbations," *Aiaa J.*, Vol. 52, No. 12, 2014, pp. 1–21.

[12]Lei, J. and Zhong, X., "Linear stability analysis of nose bluntness effects on hypersonic boundary layer transition," *Journal of Spacecraft and Rockets*, Vol. 49, No. 1, 2012, pp. 24–37.

[13]Fong, D., Wang, X., and Zhong, X., "Finite roughness effect on modal growth of a hypersonic boundary layer," *50th AIAA Aerospace Sciences Meeting including the New Horizons Forum and Aerospace Exposition*, January, 2012, pp. 1–27.

[14]Malik, M. R., "Numerical methods for hypersonic boundary layer stability," *J. Comput. Phys.*, Vol. 86, No. 2, 1990, pp. 376–413.

[15]Casper, K. M., Beresh, S. J., Henfling, J. F., Spillers, R. W., Pruett, B. O. M., and Schneider, S. P., "Hypersonic Wind-Tunnel Measurements of Boundary-Layer Transition on a Slender Cone," *AIAA Journal*, Vol. 54, No. 4, 2016, pp. 1250–1263.

[16]Casper, K. M., Beresh, S. J., Henfling, J., and Spillers, R. W., "Fluid-Structure Interactions using Controlled Disturbances on a Slender Cone at Mach 8," *54th AIAA Aerospace Sciences Meeting*, January, 2016, pp. 1–18.

[17]Mack, L. M., "Boundary Layer Linear Stability Theory," Tech. Rep., 1984.

[18]Ma, Y. and Zhong, X., "Receptivity of a supersonic boundary layer over a flat plate. Part 1. Wave structures and interactions," *Journal of Fluid Mechanics*, Vol. 488, 2003, pp. 31–78.

[19]Tang, Q., Zhu, Y., Chen, X., and Lee, C., "Development of second-mode instability in a Mach 6 flat plate boundary layer with two-dimensional roughness," *Physics of Fluids*, Vol. 27, No. 6, 2015.